Study on wind-induced vibration behavior of railway catenary in spatial stochastic wind field based on nonlinear finite element procedure

Song, Yang; Liu, Zhigang; Duan, Fuchuan; Lu, Xiaobing; Wang, Hongrui

DOI
10.1115/1.4037521

Publication date
2018

Document Version
Accepted author manuscript

Published in
Journal of Vibration and Acoustics

Study on Wind-Induced Vibration Behavior of Railway Catenary in Spatial Stochastic Wind Field Based on Nonlinear Finite Element Procedure

Article *in* Journal of Vibration and Acoustics · August 2017

DOI: 10.1115/1.4037521

Yang Song
Southwest Jiaotong University

Zhigang Liu
Southwest Jiaotong University

Fuchuan Duan
Southwest Jiaotong University

Xiaobing Lu
Southwest Jiaotong University

Journal of Vibration and Acoustics. Received January 15, 2017;
Accepted manuscript posted August 8, 2017. doi:10.1115/1.4037521

Study on Wind-induced Vibration Behaviour of Railway Catenary in Spatial Stochastic Wind Field Based on Nonlinear Finite Element Procedure

Yang Song
School of Electrical Engineering, Southwest Jiaotong University
Chengdu 610031, Sichuan, PR China
e-mail: y.song_gabrielle@outlook.com

Zhigang Liu[1]
School of Electrical Engineering, Southwest Jiaotong University
Chengdu 610031, Sichuan, PR China
e-mail: liuzg_cd@126.com

Fuchuan Duan
School of Electrical Engineering, Southwest Jiaotong University
Chengdu 610031, Sichuan, PR China
e-mail: duanfc_cd@163.com

Xiaobing Lu
School of Electrical Engineering, Southwest Jiaotong University
Chengdu 610031, Sichuan, PR China
e-mail: hello.lxb@163.com

Hongrui Wang
Section of Road and Railway Engineering, Delft University of Technology
Delft 2628CN, The Netherlands
e-mail: soul_wang0@163.com

[1]Corresponding author

Abstract

Due to its long-span structure and large flexibility, an electrified railway catenary is very sensitive to environmental wind load, especially the time-varying stochastic wind, which may lead to a strong forced vibration of contact line and deteriorate the current collection quality of the pantograph-catenary system. In this paper, in order to study the wind-induced vibration behaviour of railway catenary, a nonlinear finite element procedure is implemented to construct the model of catenary, which can properly describe the large nonlinear deformation and the non-smooth nonlinearity of dropper. The spatial stochastic wind field is developed considering the fluctuating winds in along-wind, vertical-wind and cross-wind directions. Using the empirical spectrums suggested by Kaimal, Panofsky and Tieleman, the fluctuating wind velocities in three directions are generated considering the temporal and spatial correlations. Based on fluid-induced vibration theory, the model of fluctuating forces acting on catenary are developed considering the spatial characteristics of catenary. The time-domain and frequency-domain analyses are conducted to study the wind-induced vibration behaviour with different angles of wind deflection, different angles of attack as well as different geometries of catenary. The effect of spatial wind load on contact force of pantograph-catenary system is also investigated.

Keywords: high-speed railway; catenary; stochastic wind; finite element method; computational fluid dynamics; pantograph-catenary interaction; contact force

1. Introduction

Overhead Contact Line System also called catenary is constructed along the electrified railway road, which is responsible for the transmission of the electric energy to the locomotive via a pantograph. Due to the long span and large flexibility, the wind load may cause a strong vibration of the catenary and definitely deteriorate the contact quality of the pantograph-catenary, as well as aggravate the fatigue of the contact wire. With the rapid expansion of the high-speed railway industry in China, the high-frequency buffeting of catenary caused by the short-frequency stochastic wind has been a serious issue in limiting the train's highest driving speed, which can be frequently observed in real railway lines, especially in some Newly-built high-speed railways, such as Wuhan-Guangzhou passenger special line and Beijing-Tianjin inter-city line. The dramatic wind-induced vibration of the contact line is able to produce a non-negligible detriment to the pantograph-catenary interaction, and even lead to the separation between the pantograph collector and the contact wire. However, the relevant studies on wind-induced vibration of catenary were rarely reported. Most of the previous studies were focused on the revelation of the pantograph-catenary dynamics [1-3] without wind loads. Based on the analysis results, the optimizations of pantograph-catenary were conducted for speed upgrade of existing lines [4-7]. In order to obtain more realistic simulation results, hardware-in-the-loop techniques [8-10] and full-scale experiments [11-12] were implemented to realize the hybrid simulation and verification of pantograph-catenary interaction. Considering the external perturbations, the vertical excitation of vehicle-track [13-14], the friction between the pantograph collector and contact wire [15], the aerodynamics of pantograph [16], as well as the irregularities of contact line [17-18] were included to evaluate the contact quality of pantograph-catenary system. Considering more complex operation conditions, the multiple-pantograph interaction with catenary was performed [19], and the optimal interval of double pantographs was suggested [20]. In order to improve the simulation accuracy and efficiency of pantograph-catenary interaction, the geometrical nonlinearities [21-23] of catenary wires were introduced in modelling pantograph-catenary system, and some new algorithms [24-25] were developed to facilitate the solution procedure of pantograph-catenary interaction. In order to improve the current collection quality of pantograph-catenary, various control strategies of pantograph were performed [26-29].

For the study on wind-induced vibration of catenary, it is worthwhile to mention the works done by Pombo et al [14, 30] and Song et al [31]. In [30], the time-histories of fluctuating wind velocity in vertical and lateral directions were generated by empirical spectrums. Considering the wind-structure interaction, the stochastic wind loads were exerted on the catenary to evaluate its effect on the pantograph-catenary interaction. In [14], the wind load acting on the pantograph-catenary was developed considering multiple-pantograph interactions. The work in [31] proposed a 2D stochastic wind field for railway catenary. The wind-induced behaviour of catenary was studied considering different wind velocities and angles of attack. The results show that the stochastic wind load may cause a strong forced vibration of contact line and exert a non-negligible effect on the pantograph-catenary interaction. However, there are still some limitations in previous literatures as follows:

(1) The stochastic wind component in cross-wind direction may affect the wind-induced vibration behaviour due to the spatial characteristics of catenary. In addition, the varying of angle of wind deflection cannot be considered by using a traditional 2D wind field. A 3D stochastic wind field along the railway catenary should be

constructed considering the fluctuating wind in different directions.

(2) The effect of geometrical parameters of catenary on the wind-induced vibration behaviour has not been investigated in the previous studies, which serves as the foundation of the future wind-resistant design of the catenary.

Normally the wind at a given location can be divided into a steady wind and stochastic wind component [32]. The steady wind flows in a stable direction with a constant speed. In contrast, the stochastic wind component is a time-dependent 3D sequence. In order to easily describe the complicated behaviour of the stochastic wind, three directions of the stochastic wind components are generally determined according to the flowing direction of the steady wind, which are the along-wind, cross-wind and vertical wind directions. The first component of stochastic wind shares the same direction with the steady wind, whose velocity is normally quite bigger than other two components. So in some literatures, only this stochastic wind component is considered to study the structural dynamics under wind load, such as [30, 33]. It should be noted that Pombo and Ambrósio et al. [30] conducted the first attempt to study the effect of wind on pantograph-catenary on this idea. In order to simulate the along-wind stochastic wind velocity, some scholars proposed empirical spectrums according to the experimental data, such as the famous Kamail spectrum [34]. The second component of stochastic wind is the vertical-wind stochastic wind, whose direction is perpendicular to the steady wind in vertical direction (with respect to long-span structure). The empirical spectrum for vertical stochastic wind proposed by Panofsky [35] is the most popular one widely used in different engineering backgrounds. The third one is the cross-wind stochastic wind, which is in the shear direction of the steady wind *U*. Some scholars proposed the empirical spectrum for this longitudinal component, such as Tieleman spectrum [36].

So in this paper, different to the 2D wind field in previous studies, a 3D wind filed is constructed along the high-speed railway catenary. The stochastic wind velocities in the along-wind, cross-wind and vertical-wind directions are generated considering the spatial and temporal correlations. The aerodynamic forces acting on catenary wires are derived according to fluid-induced vibration theory. The aerodynamic coefficients of the contact line cross-section are calculated by CFD. Using a nonlinear finite element catenary model, the wind-induced vibration response is analysed with different angles of wind direction, angles of attack and wind velocities. The effect of catenary geometrical structure on wind-induced vibration response is also studied. In combination with a multibody pantograph model, the pantograph-catenary interaction is performed to evaluate the effect of wind load on the contact force.

2. Spatial nonlinear catenary model

As illustrated in [31], a nonlinear 3D catenary model that is able to describe the geometrical nonlinearities of messenger/contact lines and the non-smooth nonlinearities of droppers is the necessity for studying the wind-induced vibration behaviour. In this paper, the nonlinear finite element procedure illustrated in [21] is adopted to model the catenary, in which, the contact and messenger lines are modelling by flexible cable element, and the droppers connecting the messenger and contact lines are modelled by nonlinear truss elements as shown in Figure 1. The bending stiffness of the contact/messenger wire is neglected. The geometrical nonlinearities of the messenger and contact lines and the non-smooth nonlinearities of droppers are described by updating the stiffness matrix at each time instant based on the response obtained in previous time step. Several numerical examples in [21] have been conducted to verify the validation of the static configuration according to the newest benchmark results [37] proposed by many experts in this research field. And the dynamic performance of the present model has been verified according to EN 50318 and the Siemens simulation report [38] in [21]. The results in [26, 31] indicate that the present model is able to properly describe the wind-induced vibration behaviour in a 2D stochastic wind field.

The geometrical parameters of catenary (in China Beijing-Tianjin inter-city line) shown in Table 1 [38] are adopted to construct the catenary model. As for the damping distribution, damping parameters ($\alpha = 0.062$ and $\beta = 6.13\times10^{-6}$) summarized in [12] are adopted. The A 10-span high-speed catenary model is established in this paper.

3. Establishment of spatial stochastic wind field

As illustrated in Figure 2, *U* is the steady wind velocity. u_{h} is the stochastic wind velocity in the along-wind direction. u_{p} is the stochastic wind velocity in the cross-wind direction. u_{v} is the stochastic wind velocity in the vertical-wind direction. To facilitate the description, a spatial coordinate system is established, in which the X-axis is along the railway road (along the catenary). The Y-axis and Z-axis are perpendicular to the X-axis in lateral and vertical directions, respectively. On the other hand, two planes are defined. The first one is determined by the steady wind *U* and X-axis (see plane 1). The second one is determined by the steady wind *U* and Z-axis (see plane 2). The direction of steady wind *U* is determined by two angles. The first one is the angle γ between the steady wind *U* and the X-axis as shown in plane 1, which is called the angle of wind deflection in this paper. The other one is the angle φ between the steady wind *U* and the Z-axis as shown in plane 2. The direction of u_{h} is identical to the steady wind *U*. The direction of u_{p} is perpendicular to the steady wind *U* in plane 1. Similarly the direction of u_{v} is perpendicular to the steady wind *U* in plane 2. In this section, the 3D stochastic wind field along the catenary is constructed. In Section 3.1, the time-histories of stochastic wind velocity in different directions are generated. In Section 3.2, the aerodynamic forces acting on contact and messenger lines are derived. In Section 3.3, the aerodynamic coefficients are calculated.

3.1 Generation of stochastic wind velocities

The empirical formulas for stochastic wind velocity spectrum suggested by Kaimal [34], Panofsky [35] and Tieleman [36] are adopted to generate the stochastic wind velocities in the along-wind, cross-wind and vertical-wind directions, whose explicit expressions are shown in Table 2. $S_{\mathrm{h}}(z,n)$, $S_{\mathrm{p}}(z,n)$ and $S_{\mathrm{v}}(z,n)$ are the spectrums for the stochastic wind velocities in three directions, respectively. n is the frequency of the stochastic wind; $\overline{v}_{\mathrm{z}}$ is the steady wind velocity at the reference height z .

A Four-orders AR model [39] is adopted to simulate the time history of stochastic wind velocity in each direction by the empirical spectrum. The stochastic wind velocity $V(\mathbf{X},\mathbf{Y},\mathbf{Z},t)$ of all spatial points at the time instant *t* can be expressed by

$$\begin{gathered} V(\mathbf{X},\mathbf{Y},\mathbf{Z},t) = -\sum_{i=1}^{4} \boldsymbol{\varphi}_i V(\mathbf{X},\mathbf{Y},\mathbf{Z},t-i\Delta t) + \mathbf{N}(t) \\ \mathbf{X} = [x_1, x_2, \cdots, x_m]^{\mathrm{T}} \\ \mathbf{Y} = [y_1, y_2, \cdots, y_m]^{\mathrm{T}} \\ \mathbf{Z} = [z_1, z_2, \cdots, z_m]^{\mathrm{T}} \end{gathered} \tag{1}$$

where, m is the total number of the spatial points. $\mathbf{X}$, $\mathbf{Y}$ and $\mathbf{Z}$ are the spatial position vector. Δt is the time step. The autoregressive coefficient matrix $\boldsymbol{\varphi}_i$ and random sequence $\mathbf{N}_k(t)$ are determined as follows:

According to the Wiener-Khinchin equation [40], the correlation function of two spatial points can be expressed as：

$$R_{gh}(t) = \int_0^\infty S_{gh}(f)\cos(2\pi f t)\, d\omega \qquad g,h = 1,2,\cdots,m \tag{2}$$

The correlation function matrix can be written as：

$$R(j\Delta t) = \begin{bmatrix} R_{11}(j\Delta t) & R_{12}(j\Delta t) & \cdots & R_{1n}(j\Delta t) \\ R_{21}(j\Delta t) & R_{22}(j\Delta t) & \cdots & R_{2n}(j\Delta t) \\ \vdots & \vdots & \cdots & \vdots \\ R_{n1}(j\Delta t) & R_{n2}(j\Delta t) & \cdots & R_{nn}(j\Delta t) \end{bmatrix} \tag{3}$$

in which, $j = 1,2,\cdots,p$. $\boldsymbol{\varphi}_i$ is determined by the following equation.

$$R(j\Delta t) = \sum_{i=1}^{p} R[(j-i)\Delta t]\boldsymbol{\varphi}^T{}_i \tag{4}$$

Thus, the following relationship can be achieved.

$$R(0) = \sum_{i=1}^{p} \boldsymbol{\varphi}_i R(\mathrm{i}\,\Delta t) + R_N \tag{5}$$

Through the Cholesky decomposition for $\mathbf{R}_N$, $\mathbf{R}_N = \mathbf{L}\mathbf{L}^{\mathrm{T}}$. So $\mathbf{N}(t)$ is determined as

$$\mathbf{N}(t) = \mathbf{L}\bullet\mathbf{Q}(t) \tag{6}$$

in which, $\mathbf{Q}(t) = [\mathbf{Q}_1(t), \mathbf{Q}_2(t)\cdots\mathbf{Q}_n(t)]^{\mathrm{T}}$. $\mathbf{Q}_k(t)$ is the normal random sequence independent to each other.

In this simulation, the longitudinal interval is 10m. The fluctuating wind velocities acting on 102 points of both messenger and contact wires are generated in three directions. Figure 3 shows the simulation results of wind velocities acting on the 5th and 59th points, in which the steady wind velocity is 20m/s. It can be seen that a significant difference of the velocity time-history in each point from others can be clearly observed due to the temporal and spatial stochastics. The validation can be verified by the good agreement between the auto-power and the target spectrums.

Journal of Vibration and Acoustics. Received January 15, 2017;
Accepted manuscript posted August 8, 2017. doi:10.1115/1.4037521

3.2 Derivation of aerodynamic forces

To facilitate the determination of the aerodynamic forces acting on the catenary, two coordinate systems are defined: X_g-O_g-Y_g and X_g'-O_g'-Y_g', as illustrated in Figure 4 (a). X_g-axis and Y_g-axis are the projections of X-axis and Y-axis on the Plane 1. X_g'-O_g'-Y_g' is the corresponding coordinate system modified by the stagger value. In X_g-O_g-Y_g, considering the angle of wind deflection γ, the equivalent wind load in X_g-O_g-Y_g can be obtained as:

$$\begin{cases} u_{\mathrm{X}} = u_{\mathrm{h}} \cos\gamma + u_{\mathrm{p}} \sin\gamma \\ u_{\mathrm{Y}} = -u_{\mathrm{p}} \cos\gamma + u_{\mathrm{h}} \sin\gamma \\ u_{\mathrm{Z}} = u_{\mathrm{v}} \\ U_{\mathrm{X}} = U\cos\gamma \\ U_{\mathrm{Y}} = U\sin\gamma \end{cases} \tag{7}$$

Then transferring to X_g'-O_g'-Y_g', the effective wind loads can be obtained considering the effect of stagger value (angle δ).

$$\begin{cases} u'_{\mathrm{X}} = u_{\mathrm{X}} \cos\delta + u_{\mathrm{Y}} \sin\delta \\ u'_{\mathrm{Y}} = -u_{\mathrm{X}} \sin\delta + u_{\mathrm{Y}} \cos\delta \\ u'_{\mathrm{Z}} = u_{\mathrm{Z}} \\ U'_{\mathrm{X}} = U_{\mathrm{X}} \cos\delta + U_{\mathrm{Y}} \sin\delta \\ U'_{\mathrm{Y}} = -U_{\mathrm{X}} \sin\delta + U_{\mathrm{Y}} \cos\delta \end{cases} \tag{8}$$

in which u'_{X}, u'_{Y} and u'_{Z} are the equivalent stochastic wind velocities in X_g'-O_g'-Y_g' coordinate system. U'_{X} and U'_{Y} are the corresponding equivalent steady wind velocities. The angle δ is introduced by the stagger value, which is determined by the span length L_{p} and the stagger value L_{st} as

$$\delta = \pm\arctan\left(\frac{2L_{\mathrm{st}}}{L_{\mathrm{p}}}\right) \tag{9}$$

It should be noted that the components of wind load along the X'-axis make no contribution to the wind-induced vibration, so U'_{X} and u'_{X} in Eq. (8) can be ignored.

Figure 4 (b) shows the schematic of one contact line section subjected to the wind load components u'_{Y}, u'_{Z} and U'_{Y}. α_0 is the initial angle of attack, which is determined by the two angles φ and γ according to the spatial geometrical correlation:

$$\alpha_0 = \arcsin\left(\frac{\sin\varphi}{\sin\gamma}\right) \tag{10}$$

When the wind load flows against the contact line with an angle of attack , the lift F_{L} and drag F_{D} acting on this section can be written by [31]

$$F_{\mathrm{L}} = \frac{1}{2}\rho_{\mathrm{air}} U_{\mathrm{r}} L C_{\mathrm{L}}\left(\alpha_0\right) \tag{11a}$$

$$F_{\mathrm{D}} = \frac{1}{2}\rho_{\mathrm{air}} U_{\mathrm{r}} L C_{\mathrm{D}}\left(\alpha_0\right) \tag{11b}$$

in which ρ_{air} is the air density; L is the length of contact wire. $C_{\mathrm{L}}\left(\alpha_0\right)$ and $C_{\mathrm{D}}\left(\alpha_0\right)$ are the lift and drag coefficients. U_{r} is the effective wind velocity. A dynamic wind angle β is caused by the movement of the contact line in fluid, which can lead to the change of the angle of attack. So the real aerodynamic forces F_{Lr} and F_{Dr}, and the effective angle of attack α_{r} can be expressed by

$$F_{\mathrm{Lr}} = \frac{1}{2}\rho_{\mathrm{air}} U_{\mathrm{r}} L C_{\mathrm{L}}\left(\alpha_{\mathrm{r}}\right) \tag{12a}$$

$$F_{\mathrm{Dr}} = \frac{1}{2}\rho_{\mathrm{air}} U_{\mathrm{r}} L C_{\mathrm{D}}\left(\alpha_{\mathrm{r}}\right) \tag{12b}$$

$$\alpha_{\mathrm{r}} = \alpha_0 + \beta \tag{12c}$$

where the dynamic wind angle β and the effective wind velocity U_{r} can be written by

$$\beta = \arctan\left(\frac{u'_{\mathrm{Z}} - v_{\mathrm{Z}}}{U'_{\mathrm{Y}} + u'_{\mathrm{Y}} - v_{\mathrm{Y}}}\right) \tag{13a}$$

$$U_{\mathrm{r}} = \sqrt{\left(u'_{\mathrm{Z}} - v_{\mathrm{Z}}\right)^2 + \left(U'_{\mathrm{Y}} + u'_{\mathrm{Y}} - v_{\mathrm{Y}}\right)^2} \tag{13b}$$

where v_{Z} and v_{Y} are the velocities of the contact line section in the vertical-wind and along-wind directions, which can be calculated by

$$\begin{cases} v_{\mathrm{Y}} = v_{\mathrm{y}} \cos\alpha_{\mathrm{r}} + v_{\mathrm{z}} \sin\alpha_{\mathrm{r}} \\ v_{\mathrm{Z}} = v_{\mathrm{z}} \cos\alpha_{\mathrm{r}} - v_{\mathrm{y}} \sin\alpha_{\mathrm{r}} \end{cases} \tag{14}$$

in which v_{y} and v_{z} are the lateral and vertical velocities of contact line section in the global FEM coordinate system, which can be obtained from the calculation results in each time step. It should note that the effective angle of attack α_{r} is determined by v_{Z} and v_{Y}, which are also simultaneously determined by α_{r}. This is a significant fluid-structure interaction problem. A numerical iteration procedure is employed to deal with this problem. The main idea is to use the effectively angle of attack α_{r} obtained in previous cycle to formulate the wind excitation and calculate the structural response for next cycle until the convergence is satisfied.

After obtaining the aerodynamic forces F_{Lr} and F_{Dr} according to Eq. (11-14), the aerodynamic forces which can be applied on the FEM model in the global coordinate system (X-O-Y) are obtained as follows:

$$F_{\mathrm{x}} = \left(F_{\mathrm{Dr}} \cos\alpha_{\mathrm{r}} - F_{\mathrm{Lr}} \sin\alpha_{\mathrm{r}}\right)\sin\delta \tag{15a}$$

$$F_{\mathrm{y}} = \left(F_{\mathrm{Dr}} \cos\alpha_{\mathrm{r}} - F_{\mathrm{Lr}} \sin\alpha_{\mathrm{r}}\right)\cos\delta \tag{15b}$$

$$F_{\mathrm{z}} = F_{\mathrm{Dr}} \sin\alpha_{\mathrm{r}} + F_{\mathrm{Lr}} \cos\alpha_{\mathrm{r}} \tag{15c}$$

The above derivation is to determine the aerodynamic forces acting on contact line. A similar procedure can be utilized to obtain the aerodynamic forces acting on messenger line.

3.3 Calculation of aerodynamic coefficients

The CFD software —— Fluent is utilized to simulate the streaming around the contact line cross-section, and calculate the aerodynamic coefficients of the contact/messenger line with different wind velocities and angles of attack. The CFD model for the contact line section is established. The mesh property and the boundary conditions are defined according to [31]. The calculation results of the aerodynamic coefficients of contact line are shown in Figure 5. It can be seen that the drag coefficient C_D does not experience a large change versus angle of attack. In contrast, the lift coefficient C_L shows a sharp change around the angle of attack 40° due to the effect of groove existing on the contact line cross-shape. The aerodynamic coefficients of the messenger line are also calculated in this way, whose cross-shape is considered perfectly circular from an ideal view.

4. Analysis of the wind-induced vibration of catenary

Substituting the aerodynamic coefficients and the time-histories of fluctuating wind velocities into the aerodynamic forces derived in Section. 3.2, the spatial wind field along the catenary is established. In this section, the wind-induced vibration response is generally analysed firstly. Then the effects of the angle of wind deflection and angle of attack on the vibration response are analysed, respectively.

4.1 General analysis of wind-induced vibration response

Firstly, the wind-induced vibration response is analysed generally. The simulation conditions are defined as: U = 10m/s or 20m/s; α_0= 20° and γ= 80°. The results of maximum lateral deviation of the contact line in the 5th and 6th spans are plotted in Figure 6 (a), and the corresponding results of maximum vertical deviation are shown in Figure 6 (b). For each span, the maximum lateral and vertical deviations appear at the mid-span point. For the vertical vibration, the wind deviation shows a significant decrease at each dropper point, due to the large lumped stiffness. The lateral and vertical displacements of the mid-point (of the 5th span) are shown in Figure 7 (a-b) respectively. It can be seen that the vibration with U=20m/s is much stronger than that with U=10m/s. In Figure 8 (a-b), the spectrums of the lateral and vertical vibration are estimated through the Yule-Walker algorithm, in which the mean value of response has been removed to reduce the effect of the static wind deviation on the spectrum estimation results. The spectra peak of the lateral displacement spectrum concentrates at around the first-order natural frequency which are shown in Table 3. The first peak may be excited by the mean value remaining in the signal, and the limitations of the Fast Fourier Transform. A peak resonant vibration can be significantly observed from the spectrum of the catenary vibration response caused by the spatial stochastic wind.

4.2 With different angles of wind deflection

In this analysis, the boxplot of the vibration displacement is utilized to evaluate the fluctuation range of the wind-induced vibration. In this simulation, the angle of attack α_0 is defined as 20°, and the steady wind U is defined as 20m/s.

The boxplots of the lateral and vertical displacements of the mid-span point of the contact wire versus angle of wind deflection with U=20m/s are shown in Figure 9 (a-b), respectively. In each box, the central red line is the median value of the displacement, which can be used to evaluate the wind deflection caused by the steady wind. The edges of the box are the 25th and 75th percentiles. The boundaries are the maximum values of the displacement, which are used to specify the fluctuation range of the vibration caused by stochastic wind. It can be seen from

Figure 9 (a-b) that the increase of the angle of wind deflection results in a significant increase of the wind deflection (as the red line shows) in both of the lateral and vertical directions. Simultaneously the fluctuations in the lateral and vertical directions become much stronger, which may affect the current collection quality of the pantograph-catenary system more strongly.

4.3 With different angles of attack

Apart from the angle of wind deflection, the angle of attack also affects the wind-induced vibration behaviour of the contact line. In this section, the angle of wind deflection γ is defined as 80°, and the steady wind U is 20m/s. As the angle of attack cannot reach a very big value, the range of angle of attack is defined from -20°~20°. Similar to the above analysis, the boxplots of the lateral and vertical displacements of the mid-span point of the contact wire versus angle of attack with U=20m/s are shown in Figure 10 (a-b), respectively. For the lateral vibration, when the angle of attack increases from -20° to 0°, the lateral wind deflection and the fluctuation range experience sharp increases. However, it is unexpected that when the angle of attack increases from 0° to 20°, the lateral wind deflection shows a continuous increase. It is because that as the angle of attack increases closer to a vertical direction (from 0° to 20°), the value of lift coefficient C_L shows a sharp increase, as shown in Figure 5, which results in a larger wind load component in the lateral direction. For the vertical vibration, it can be seen that the negative angle of attack causes a negative wind deflection, which decreases with the wind flow closer to the horizontal direction. Accordingly a positive angle of attack is able to cause a positive wind deflection, which increases with the increase of the angle of attack. Due to the aerodynamics of the contact wire, the minimum fluctuation and deflection in vertical displacement appear at the angle of attack 10°.

5. Effect of catenary geometry on wind-induced vibration

In this section, the effect of catenary geometrical structure on the wind-induced vibration behaviour is studied, which is able to provide beneficial reference for the future wind-resistant design of catenary. As the description in Section 3.1, the temporal and spatial correlations are both considered in simulating the stochastic wind velocities. The stochastic wind velocities should be updated with the change of the geometrical structure of catenary, which may cause some randomness of the vibration response. So in this section, the boxplots may lose its efficiency in analysing the vibration response. The integration of displacement over a period of time (0~80s in this paper) is utilized to evaluate the global intensity of the wind-induced vibration. As shown in Eq. (15), b_p and b_v are the global index to evaluate the vibration intensity in lateral and vertical directions, respectively. In addition, b_g is utilized to evaluate the total vibration intensity.

$$b_p = \int_0^{t_u} \sqrt{\left(x_p(t) - x_p(0)\right)^2}\,dt \tag{16a}$$

$$b_v = \int_0^{t_u} \sqrt{\left(x_v(t) - x_v(0)\right)^2}\,dt \tag{16b}$$

$$b_g = \int_0^{t_u} \sqrt{\left(x_p(t) - x_p(0)\right)^2 + \left(x_v(t) - x_v(0)\right)^2}\,dt \tag{16c}$$

where $x_p(t)$ and $x_v(t)$ are the lateral and vertical displacements of the mid-point of the 5th span on contact wire. t_u is the upper boundary of time. The following analyses in this section are based on the same parameters of stochastic wind field: U=20m/s; α= 5°; γ= 80°.

5.1 Influence of tension

The results of the integration of displacement with U=20m/s are shown in Figure 11. b_p, b_v and b_g are totally decreased by the increase of the tension acting on the contact line. So the increase of tension acting on contact line has an effective effect in suppressing the wind-induced vibration in each direction.

Apart from the time-domain analysis, the spectrum estimation is implemented to investigate the effect of the contact line tension on the vibration response. The spectrums of the lateral and vertical displacements with U=20m/s and $\alpha_0 = 5^\circ$ are shown in Figure 12 (a) and (b). The first-order natural frequencies in both directions with different contact wire tensions are listed in Table 4. No matter in lateral or vertical direction, the spectra peak appears around the corresponding first-order frequency, which generally shows a slight decrease by the increase of tension. As well known, the upgrade of the tension class keeps the natural frequency far away from the frequency of stochastic wind, which can make a good contribution to the wind-resistant capability of catenary.

5.2 Influence of length of span

In this study, the wind-induced vibration response is analysed with different lengths of catenary span. Similar to the above analysis, the integrations of displacement versus length of span are shown in Figure 13. It can be found that b_p, b_v and b_g show continuous increases with the increase of the length of span, which results in a stronger vibration of the contact line. So the increase of the span length is able to decrease the wind-resistant capability of the catenary, and a large span should be avoided in the strong wind field. To observe the change of the power distribution in frequency-domain of the vibration response, the spectrums of the lateral and vertical displacements with different steady wind velocities are shown in Figure 14. The first-order natural frequencies in both directions with different lengths of span are listed in Table 5. It is seen that the increase of the length of span is able to lower the catenary system's natural frequency, which makes the structure more sensitive to the wind load.

5.3 Influence of stagger value

The results of integration of displacement with different stagger values (from 0 to 0.4m) are shown in Figure 15. It can be seen that b_p, b_v and b_g are not significantly changed by the small adjustment of the stagger value. As the stagger value is very small in this analysis (which cannot be a big value in reality), the influence of the stagger value on the wind-induced vibration response is totally ignorable.

In order to make sense of the effect of stagger value on the wind-induced vibration more clearly, bigger stagger values are included to conduct the following investigation. The results of integration of displacement with different bigger stagger values are shown in Figure 16. It can be seen that a bigger stagger value can effectively decrease the vibration intensity of the contact line. But in reality, the stagger value must be limited to a very small value to avoid the separation of the pantograph collector from the contact line in lateral direction. So a sizable adjustment of stagger value cannot be a feasible measure in the wind-resistant design of catenary.

6. Effect of spatial stochastic wind load on pantograph-catenary interaction

In this section, a multi-body pantograph model is included to investigate the effect of the spatial stochastic wind on the pantograph-catenary interaction. The parameters of pantograph are adopted from a DSA-type of a high-speed pantograph used in China. The contact between the contact wire and pantograph collector is realized by the penalty function method. The Newmark-β integration scheme is utilized to solve the equation of motion for the pantograph-catenary interaction. As well known, the contact force between the pantograph and the catenary is of great significance to describe the contact quality. According to EN 50367, the standard deviation of contact force is able to reflect its fluctuation, which is adopted in this analysis to evaluate the effect of the wind load on the current collection quality. In the following simulations, the results of the contact force in central two spans are adopted as the analysis object, and are filtered with the frequency of interest from 0 to 20 Hz by a type I Chebyshev IIR digital filter with second-order sections (SOS). Table 6 shows the verification of the present model according to EN50318. One significant limitation of this analysis should be pointed out that the effect of the wind load on the vehicle and pantograph is not considered.

6.1 With different angles of wind deflection

The angle of attack is chosen as 20°, and the steady wind velocity is defined as 10m/s or 20m/s. The train speed is 300km/h. The results of the contact force with different angles of wind deflection under U=20m/s are shown in Figure 17. It can be seen that the fluctuation in the contact force shows a significant increase with the increase of the angle of wind deflection closer to perpendicular direction, which is manifested by the increase of the maximum value and the decrease of the minimum value. The standard deviations of the contact force versus angle of wind deflection are shown in Figure 18. No matter with U= 10m/s or U= 20m/s, the standard deviation shows a continuous increase with the increase of the angle of wind deflection, which cause a worse current collection quality. The standard deviation of the contact force without wind load is 29.0635 N, which is very close to the value (29.4 N) with γ= 0° and U= 10m/s. So the stochastic wind load exerts totally negative effect on the contact quality of the pantograph-catenary, which becomes much stronger with the increase of the wind velocity and the angle of wind deflection closer to the perpendicular direction.

6.2 With different angles of attack

In order to observe the effect of angle of attack on the contact force of the pantograph-catenary system, the angle of wind deflection is chosen as 80°, and the steady wind velocity is 10m/s or 20m/s. The results of the contact force with different angles of attack under U= 20m/s are shown in Figure 19. The standard deviations of the contact force versus angle of attack are shown in Figure 20. Generally, the more the wind flows in a vertical direction, the worse the current collection quality becomes. When α_0 = 10°, the wind has the least effect on the vertical interaction of the pantograph-catenary interaction. This conclusion is consistent to the analysis results of the vertical vibration response affected by the angle of attack in Section 4.3.

7. Conclusions

In this paper, the wind-induced vibration behaviour of the electrified railway catenary in the spatial stochastic wind field is investigated. A high-speed railway catenary constructed in China is adopted as the analysis object, whose spatial nonlinear model is established using flexible cable and truss elements with properly considering the geometrical nonlinearity of messenger/contact line, and the non-smooth nonlinearity of dropper. The Kaimal, Panofsky and Tieleman spectrums are utilized to generate the stochastic wind velocities in the along-wind, vertical-wind and cross-wind directions based on the 4-orders AR model. The aerodynamic forces acting on the messenger and contact lines are derived based on the fluid-induced vibration theory. The aerodynamic coefficients considering the grooves existing on the contact line cross-section are calculated by CFD. Through the analysis of the wind-induced vibration response with different wind loads, different catenary geometries and its effect on the pantograph-catenary interaction, some conclusions are drawn as follows:

(1) The vibration response excited by the fluctuating wind shows significant stochastics. The maximum wind deflection appears at the mid-span point of the contact line. The spectra peak of the wind-induced vibration response concentrates at around the first natural frequency of the catenary. Not only the wind deflection but also the fluctuation in the vibration response show significant increases with the increase of the angle of wind deflection closer to perpendicular direction. The increase of the angle of attack closer to the vertical direction is able to increase the vertical wind deflection as well as the fluctuation in the vibration response. Due to the particular aerodynamics of the contact line, the increase of the angle of attack from -20° to 20° leads to a continuous increase of the lateral wind deviation.

(2) The increase of the tension and the decrease of the length of span are effective measures to decrease the wind-induced vibration intensity. The degradation of the tension class and the increase of the span length can lower the natural frequency of the catenary in both the lateral and vertical directions, which may increase the system's sensitivity to wind load. The small adjustment of the stagger value cannot largely influence the vibration response, which is not a feasible measure in the wind-resistant design of catenary.

(3) The fluctuation in the contact fore can be largely affected by the stochastic wind load. Both of the increase of the angle of wind deflection closer to the perpendicular direction and the increase of the angle of attack closer to the vertical direction can increase the fluctuation in contact force. The conclusion is consistent to the analysis of the vertical vibration excited by the stochastic wind load.

8. Discussions for future works

The future work will focus on three shortfalls in this work.

(1) The aerodynamic coefficients of the contact line should be verified through the wind tunnel experiment. In fact, the wind tunnel experiment has been conducted to measure the aerodynamic coefficients, as shown in Figure 21. The contact line model is made 10 times bigger than its original size. However, due to the old instrument, only the horizontal wind can be considered, and only the aerodynamic coefficients at the range of angle of attack ± 5° can be measured. The results are compared with the CFD results in Table 7. Two sets of results show good agreement. But this is not enough to perfectly verify the accuracy of the CFD results. In the future, a more developed wind tunnel will be utilized to measure the aerodynamic coefficients of the contact wire with different

working conditions (such as iced-line and wear, which may change the aerodynamics of the contact line). On the other hand, a field experiment for the whole catenary is necessary to be conducted for studying its wind-induced vibration behavior. So a small-scale experimental model is under construction, which will be utilized to investigate the vibration behaviour in a wind tunnel.

(2) As we know, the wind load continuously acts on the whole catenary, which is simplified to a number of discrete loads acting on finite points of catenary. And the wind load on the droppers are neglected in this paper. In the future, a CFD model for dropper will be established, and deeper investigations should be conducted to develop the aerodynamic load acting on catenary.

(3) The fluctuating wind velocities are generated based on empirical spectrums, which may not be consistent to the circumstance of a real railway line. Aiming at some railway catenaries constructed in strong wind fields in China, the stochastic wind velocities and orientations will be measured, and the spectrums for wind velocity along China railway road will be constructed to improve the simulation efficiency of the stochastic wind field.

(4) As illustrated in the works of Pombo et al [30], the wind load on pantograph and train plays a non-negligible role in influencing the pantograph-catenary interaction, which is not considered in the analysis of this work. In the future, the CFD models of pantograph components and the whole train will be established to evaluate the effect of the stochastic wind from a more general view.

Acknowledgements

This work was supported in part by the National Nature Science Foundation of China (U1434203, 51377136 and 51407147), Scientific Research and Development Program for Railway Ministry (2013J010-B), Sichuan Province Youth Science and Technology Innovation Team (2016TD0012), Excellent Doctoral Thesis Cultivation Program of Southwest Jiaotong University. The authors appreciate the reviewers' valuable comments.

References

[1] Jung, S. P., Kim, Y. G., Paik, J. S., and Park, T. W., 2012, "Estimation of dynamic contact force between a pantograph and catenary using the finite element method," Journal of Computational and Nonlinear Dynamics, **7**(4), 041006.

[2] Lopez-Garcia, O., Carnicero, A., and Maroño, J. L., 2007, "Influence of stiffness and contact modelling on catenary–pantograph system dynamics," Journal of Sound and Vibration, **299**(4), 806-821.

[3] Pombo, J., and Ambrósio, J., 2012, "Influence of pantograph suspension characteristics on the contact quality with the catenary for high speed trains," Computers & Structures, **110**, 32-42.

[4] Rønnquist, A., and Nåvik, P., 2015, "Dynamic assessment of existing soft catenary systems using modal analysis to explore higher train velocities: a case study of a Norwegian contact line system," Vehicle System Dynamics, **53**(6), 756-774.

[5] Nåvik, P., Rønnquist, A., and Stichel, S., 2016, "The use of dynamic response to evaluate and improve the optimization of existing soft railway catenary systems for higher speeds," Proceedings of the Institution of Mechanical Engineers, Part F: Journal of Rail and Rapid Transit, **230**(4), 1388-1396.

[6] Massat, J. P., Laurent, C., Bianchi, J. P., and Balmès, E., 2014, "Pantograph catenary dynamic optimisation based on advanced multibody and finite element co-simulation tools," Vehicle System Dynamics, **52**(sup1),

338-354.

[7] Kim, J. W., Chae, H. C., Park, B. S., Lee, S. Y., Han, C. S., and Jang, J. H., 2007, "State sensitivity analysis of the pantograph system for a high-speed rail vehicle considering span length and static uplift force," Journal of Sound and Vibration, **303**(3), 405-427.

[8] Schirrer, A., Aschauer, G., Talic, E., Kozek, M., and Jakubek, S., 2017, "Catenary emulation for hardware-in-the-loop pantograph testing with a model predictive energy-conserving control algorithm," Mechatronics, **41**, 17-28.

[9] Bruni, S., Bucca, G., Collina, A., and Facchinetti, A., 2012, "Numerical and hardware-in-the-loop tools for the design of very high speed pantograph-catenary systems," Journal of Computational and Nonlinear Dynamics, **7**(4), 041013.

[10] Facchinetti, A., Gasparetto, L., and Bruni, S., 2013, "Real-time catenary models for the hardware-in-the-loop simulation of the pantograph–catenary interaction," Vehicle System Dynamics, **51**(4), 499-516.

[11] Lee, J. H., Park, T. W., Oh, H. K., and Kim, Y. G., 2015, "Analysis of dynamic interaction between catenary and pantograph with experimental verification and performance evaluation in new high-speed line," Vehicle System Dynamics, **53**(8), 1117-1134.

[12] Nåvik, P., Rønnquist, A., and Stichel, S., 2016, "Identification of system damping in railway catenary wire systems from full-scale measurements," Engineering Structures, **113**, 71-78.

[13] Carnicero, A., Jimenez-Octavio, J. R., Sanchez-Rebollo, C., Ramos, A., and Such, M., 2012, "Influence of track irregularities in the catenary-pantograph dynamic interaction," Journal of Computational and Nonlinear Dynamics, **7**(4), 041015.

[14] Pombo, J., and Ambrósio, J., 2013, "Environmental and track perturbations on multiple pantograph interaction with catenaries in high-speed trains," Computers & Structures, **124**, 88-101.

[15] Qian, W. J., Chen, G. X., Zhang, W. H., Ouyang, H., and Zhou, Z. R., 2013, "Friction-induced, self-excited vibration of a pantograph-catenary system," Journal of Vibration and Acoustics, **135**(5), 051021.

[16] Kulkarni, S., Pappalardo, C. M., and Shabana, A. A., 2017, "Pantograph/catenary contact formulations," Journal of Vibration and Acoustics, **139**(1), 011010.

[17] Vo Van, O., Massat, J. P., Laurent, C., and Balmes, E., 2014, "Introduction of variability into pantograph–catenary dynamic simulations," Vehicle System Dynamics, **52**(10), 1254-1269.

[18] Wang, H., Liu, Z., Song, Y., Lu, X., Han, Z., Zhang, J., and Wang, Y., 2016, "Detection of contact wire irregularities using a quadratic time–frequency representation of the pantograph–catenary contact force," IEEE Transactions on Instrumentation and Measurement, **65**(6), 1385-1397.

[19] Pombo, J., and Ambrósio, J., 2012, "Multiple pantograph interaction with catenaries in high-speed trains," Journal of Computational and Nonlinear Dynamics, **7**(4), 041008.

[20] Liu, Z., Jönsson, P. A., Stichel, S., and Rønnquist, A., 2016, "On the implementation of an auxiliary pantograph for speed increase on existing lines," Vehicle System Dynamics, **54**(8), 1077-1097.

[21] Song, Y., Liu, Z., Wang, H., Lu, X., and Zhang, J., 2015, "Nonlinear modelling of high-speed catenary based on analytical expressions of cable and truss elements," Vehicle System Dynamics, **53**(10), 1455-1479.

[22] Tur, M., García, E., Baeza, L., and Fuenmayor, F. J., 2014, "A 3D absolute nodal coordinate finite element model to compute the initial configuration of a railway catenary," Engineering Structures, **71**, 234-243.

[23] Gregori, S., Tur, M., Nadal, E., Fuenmayor, F. J., and Chinesta, F., 2016, "Parametric model for the simulation

of the railway catenary system static equilibrium problem," Finite Elements in Analysis and Design, **115**, 21-32.

[24] Jimenez-Octavio, J. R., Carnicero, A., Sanchez-Rebollo, C., and Such, M., 2015, "A moving mesh method to deal with cable structures subjected to moving loads and its application to the catenary–pantograph dynamic interaction," Journal of Sound and Vibration, **349**, 216-229.

[25] Oumri, M., and Rachid, A., 2016, "A mathematical model for pantograph-catenary interaction," Mathematical and Computer Modelling of Dynamical Systems, **22**(5), 463-474.

[26] Song, Y., Liu, Z., Ouyang, H., Wang, H., and Lu, X., 2017, "Sliding mode control with PD sliding surface for high-speed railway pantograph-catenary contact force under strong stochastic wind field," Shock and Vibration, ahead of print.

[27] Sanchez-Rebollo, C., Jimenez-Octavio, J. R., and Carnicero, A., 2013, "Active control strategy on a catenary–pantograph validated model," Vehicle System Dynamics, **51**(4), 554-569.

[28] Pappalardo, C. M., Patel, M. D., Tinsley, B., and Shabana, A. A., 2016, "Contact force control in multibody pantograph/catenary systems," Proceedings of the Institution of Mechanical Engineers, Part K: Journal of Multi-body Dynamics, **230**(4), 307-328.

[29] Song, Y., Ouyang, H., Liu, Z., Mei, G., Wang, H., and Lu, X., 2008, "Active control of contact force for high-speed railway pantograph-catenary based on multi-body pantograph model," Mechanism and Machine Theory, **115**, 35-39.

[30] Pombo, J., Ambrósio, J., Pereira, M., Rauter, F., Collina, A., and Facchinetti, A., 2009, "Influence of the aerodynamic forces on the pantograph–catenary system for high-speed trains," Vehicle System Dynamics, **47**(11), 1327-1347.

[31] Song, Y., Liu, Z., Wang, H., Lu, X., and Zhang, J., 2016, "Nonlinear analysis of wind-induced vibration of high-speed railway catenary and its influence on pantograph–catenary interaction," Vehicle System Dynamics, **54**(6), 723-747.

[32] Di Paola, M., 1998, "Digital simulation of wind field velocity," Journal of Wind Engineering and Industrial Aerodynamics, **74**, 91-109.

[33] Yang, W., Chang, T. and Chang, C., 1997, "An efficient wind field simulation technique for bridges," Journal of Wind Engineering and Industrial Aerodynamics, **67**, 697-708.

[34] Kaimal, J.C., 1978, "Horizontal velocity spectra in an unstable surface layer," Journal of the Atmospheric Sciences, 35(1), 18-24.

[35] Panofsky, H.A. and McCormick, R.A., 1960, "The spectrum of vertical velocity near the surface," Quarterly Journal of the Royal Meteorological Society, **86**(370), 495-503.

[36] Tieleman H W. 1995, "Universality of velocity spectra," Journal of Wind Engineering and Industrial Aerodynamics, **56**, 55-69.

[37] Bruni S., Ambrósio J., Carnicero A., Cho Y., Finner L., Ikeda M., Kwon S., Massat J., Stichel S., Tur M., Zhang W., 2015, "The results of the pantograph–catenary interaction benchmark," Vehicle System Dynamics, **53**(3): 412-435.

[38] Reichmann Th., 2006, "Dynamic performance of pantograph/overhead line interaction for 4 span overlaps – TPS/OCS portion," SIEMENS, 4-21.

[39] Chen, P., Pedersen, T., Bak-Jensen, B. and Chen, Z., 2010, "ARIMA-based time series model of stochastic

Journal of Vibration and Acoustics. Received January 15, 2017;
Accepted manuscript posted August 8, 2017. doi:10.1115/1.4037521

wind power generation," IEEE Transactions on Power Systems, **25**(2), 667-676.

[40] Iannuzzi, A. and Spinelli, P., 1987, "Artificial wind generation and structural response," Journal of Structural Engineering, **113**(12), 2382-2398.

List of Figure Captions

List of Table Headings

Journal of Vibration and Acoustics. Received January 15, 2017;
Accepted manuscript posted August 8, 2017. doi:10.1115/1.4037521

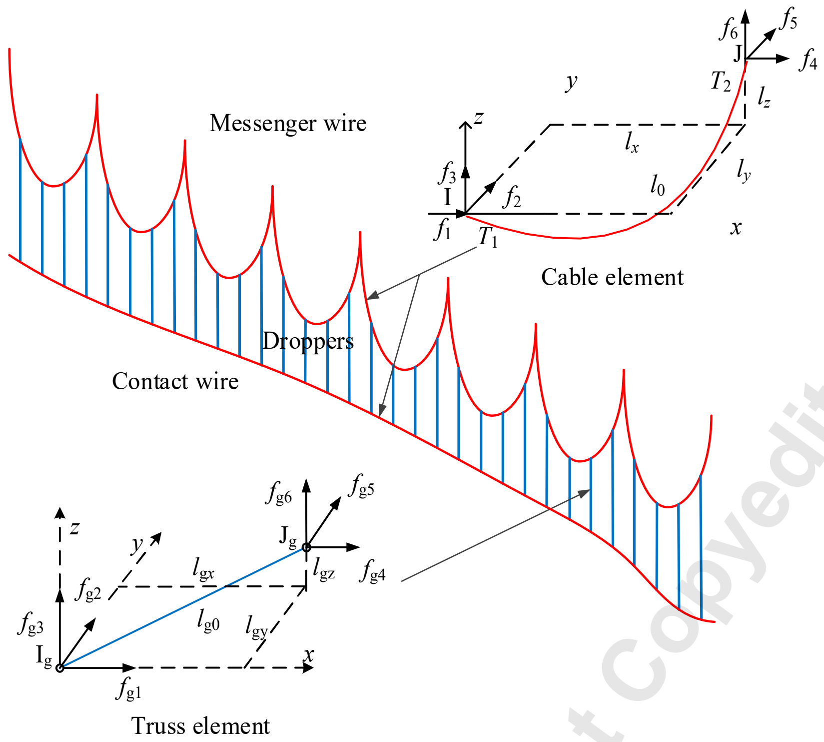

Figure 1. Nonlinear 3D catenary model

Journal of Vibration and Acoustics. Received January 15, 2017;
Accepted manuscript posted August 8, 2017. doi:10.1115/1.4037521

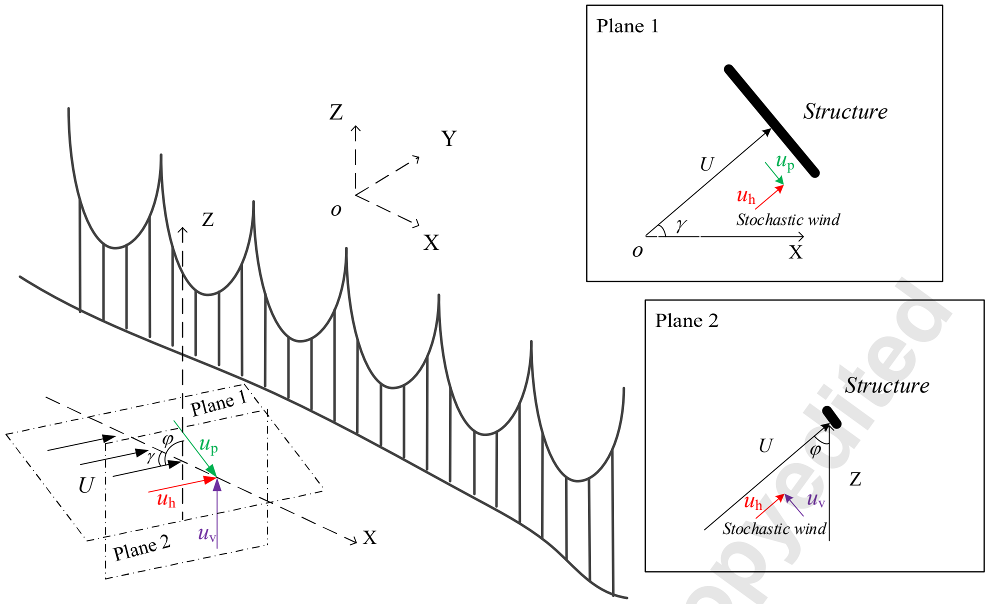

Figure 2. Schematic of spatial wind field

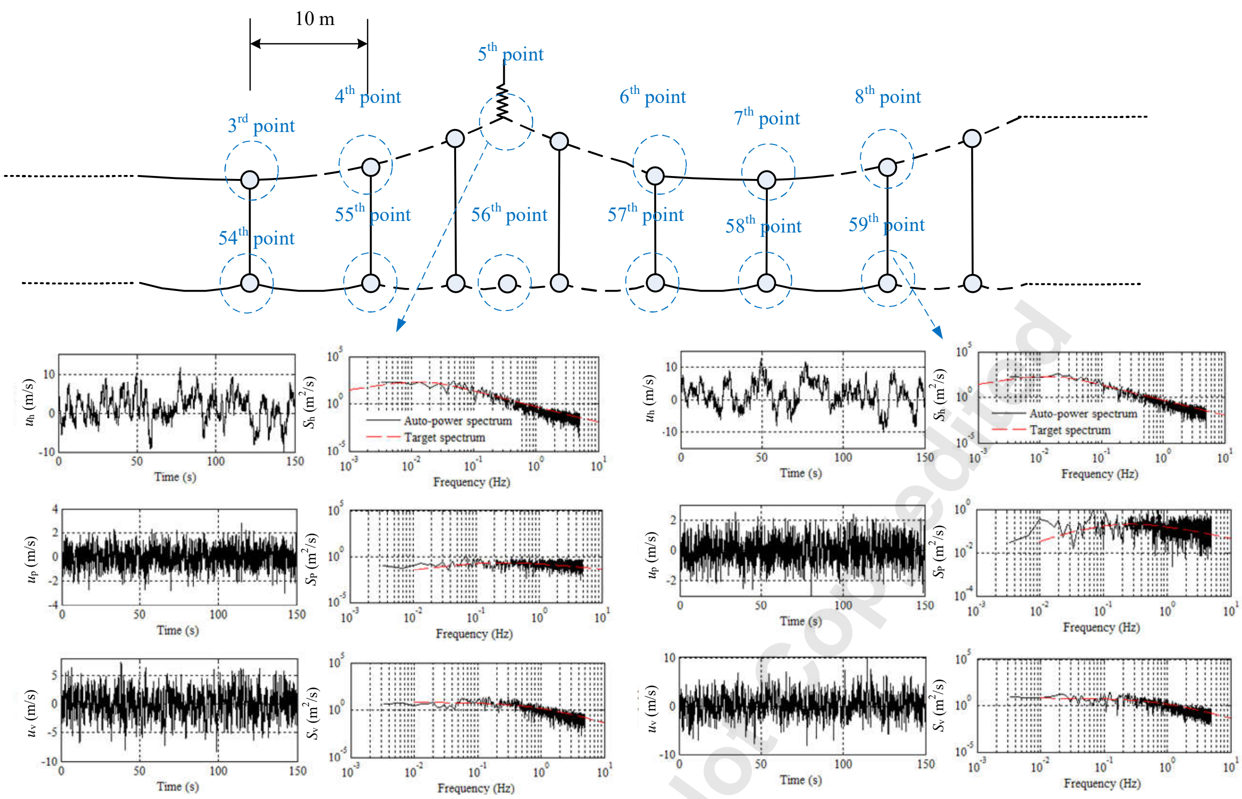

(a) Stochastic wind velocities acting on the 5th point

(b) Stochastic wind velocities acting on the 59th point

Figure 3. Stochastic wind velocities in three directions

Journal of Vibration and Acoustics. Received January 15, 2017;
Accepted manuscript posted August 8, 2017. doi:10.1115/1.4037521

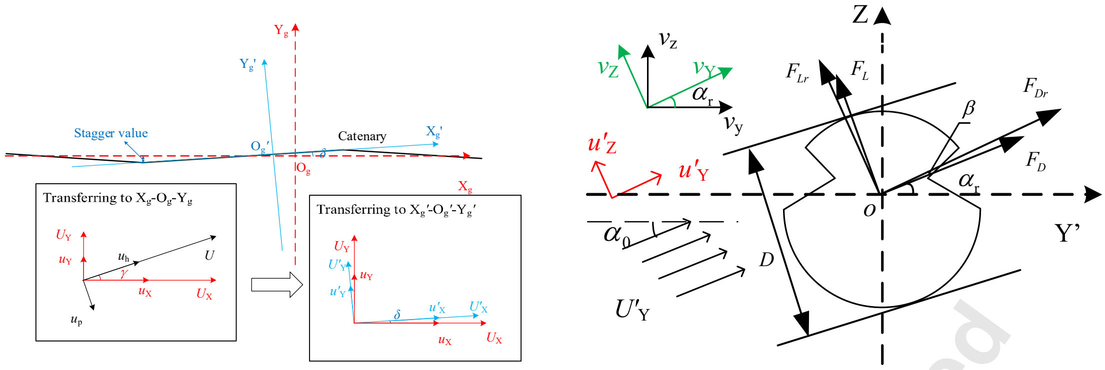

(a) Schematic of coordinate transformation (b) Schematic of contact line cross-section with wind load

Figure 4. Determination of aerodynamic forces acting on catenary

Journal of Vibration and Acoustics. Received January 15, 2017;
Accepted manuscript posted August 8, 2017. doi:10.1115/1.4037521

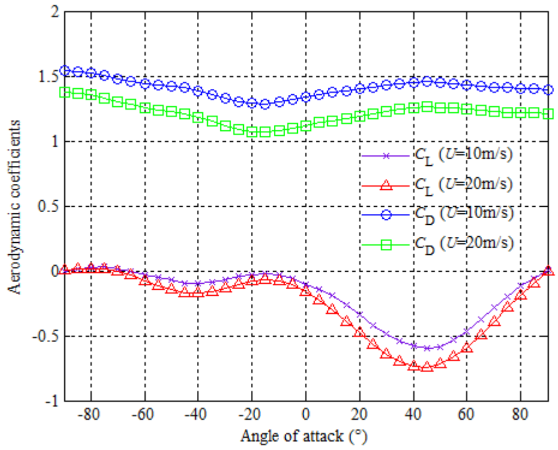

Figure 5. Calculation results of aerodynamic coefficients of contact line

Journal of Vibration and Acoustics. Received January 15, 2017;
Accepted manuscript posted August 8, 2017. doi:10.1115/1.4037521

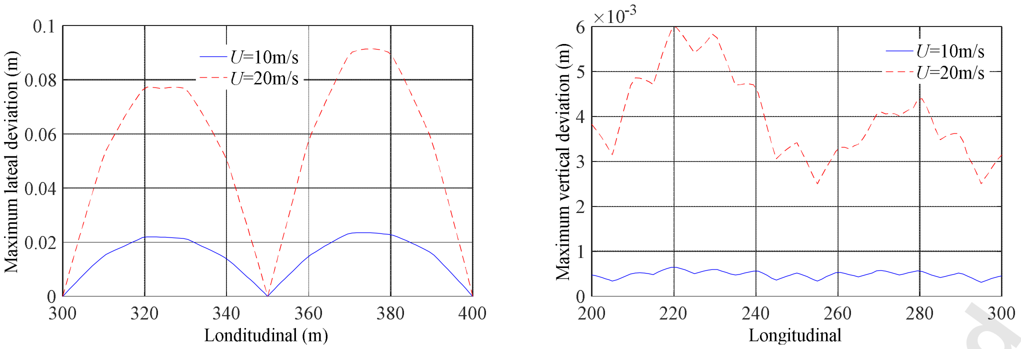

(a) Maximum lateral deviation (b) Maximum vertical deviation

Figure 6. Results of maximum deviation of contact line

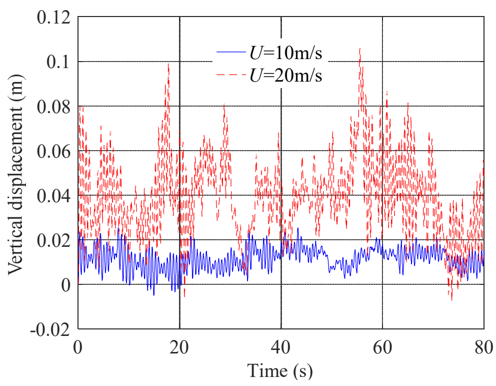

(a) Lateral vibration

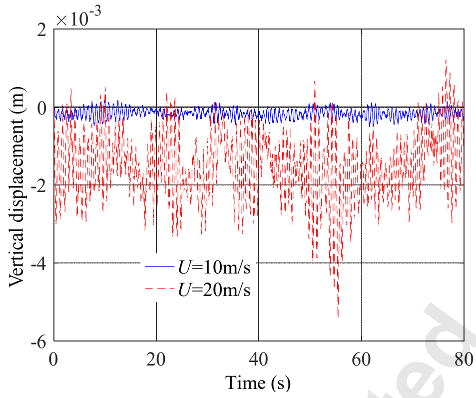

(b) Vertical vibration

Figure 7. Results of vibration response of mid-points

Journal of Vibration and Acoustics. Received January 15, 2017;
Accepted manuscript posted August 8, 2017. doi:10.1115/1.4037521

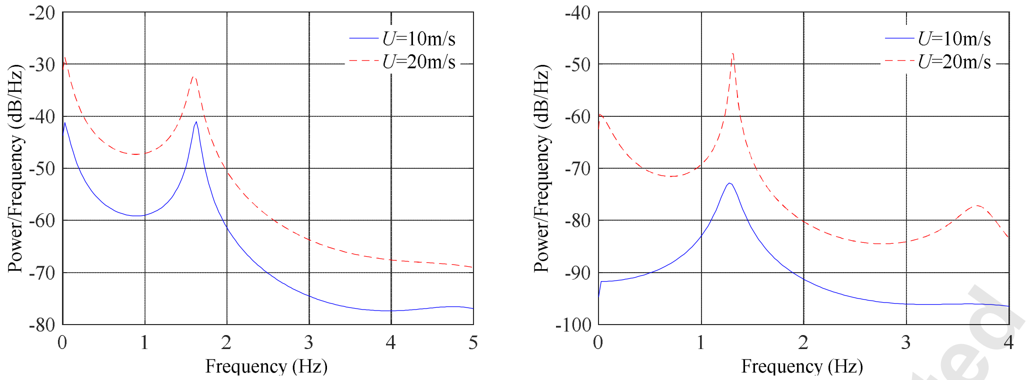

Figure 8. Spectrums of the vibration response

Journal of Vibration and Acoustics. Received January 15, 2017;
Accepted manuscript posted August 8, 2017. doi:10.1115/1.4037521

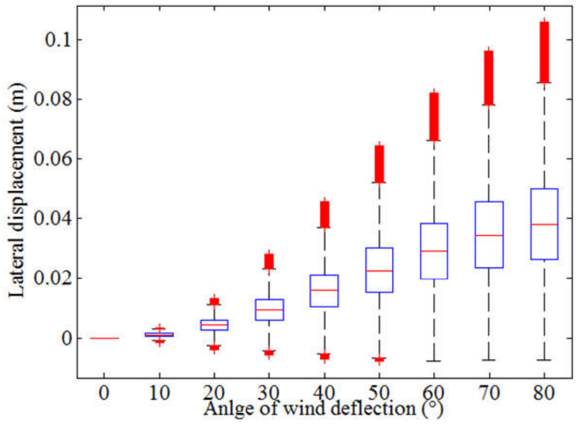

(a) Lateral vibration

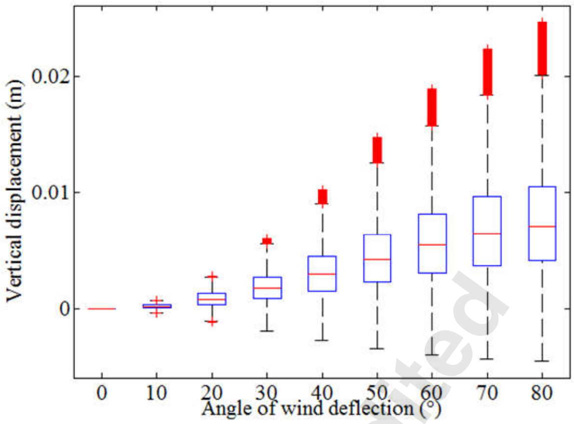

(b) Vertical vibration

Figure 9. Boxplots of the vibration response with different angles of wind deflection (U= 20m/s)

Journal of Vibration and Acoustics. Received January 15, 2017;
Accepted manuscript posted August 8, 2017. doi:10.1115/1.4037521

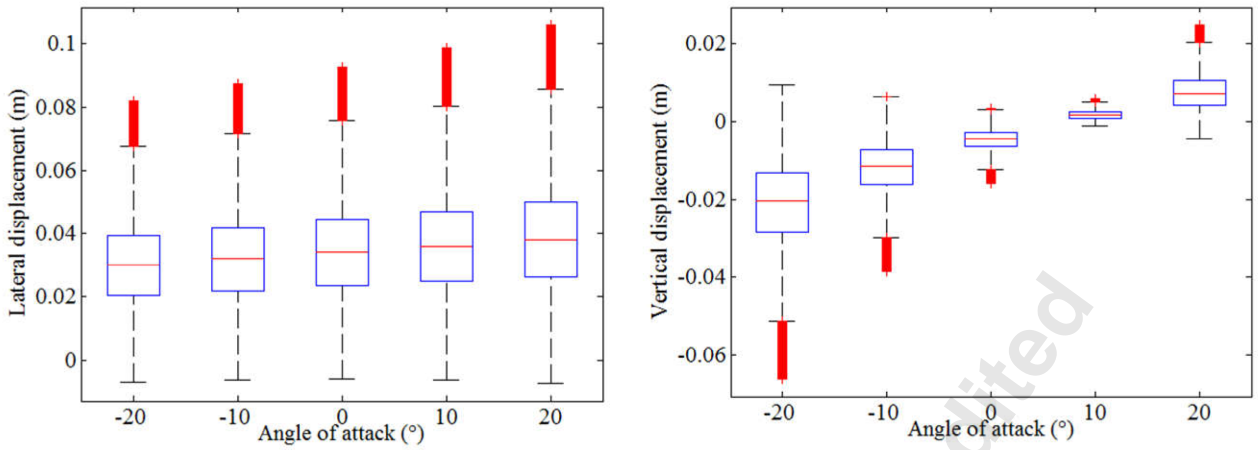

(a) Lateral vibration (b) Vertical vibration

Figure 10. Boxplots of the vibration response with different angles of attack (*U*= 20m/s)

Journal of Vibration and Acoustics. Received January 15, 2017;
Accepted manuscript posted August 8, 2017. doi:10.1115/1.4037521

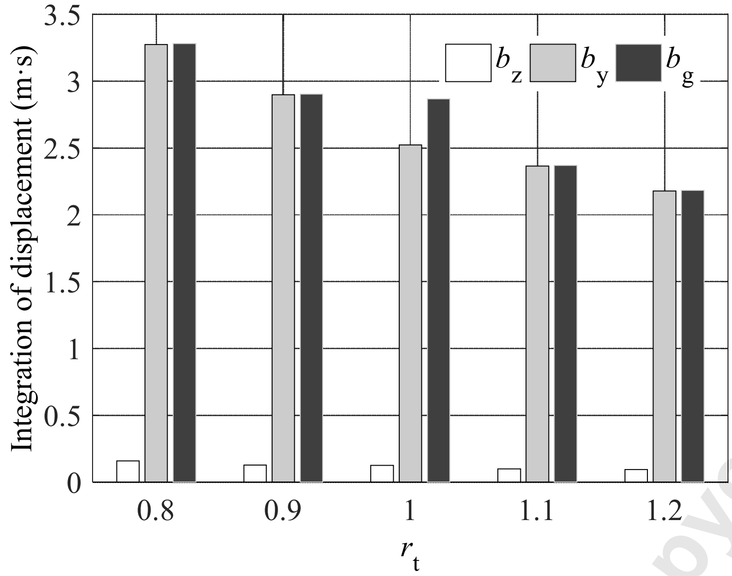

Figure 11. Results of integration of displacement with different tensions

Journal of Vibration and Acoustics. Received January 15, 2017;
Accepted manuscript posted August 8, 2017. doi:10.1115/1.4037521

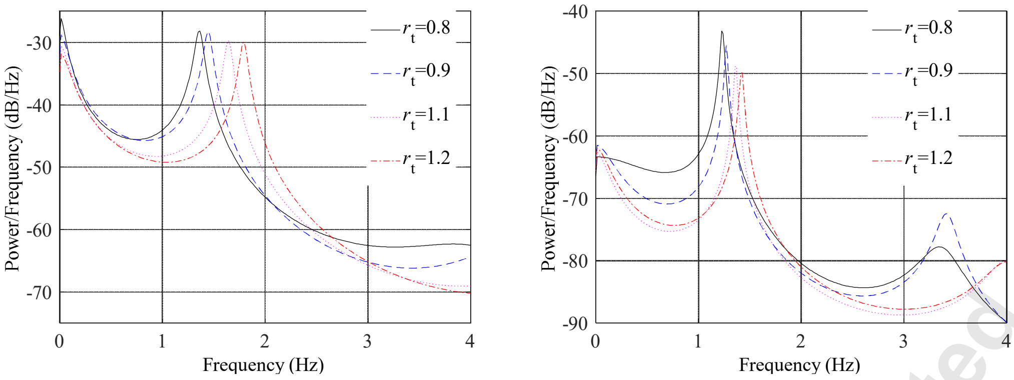

(a) Lateral vibration (b) Vertical vibration

Figure 12. Spectrums of the vibration response with different tensions with U= 20m/s

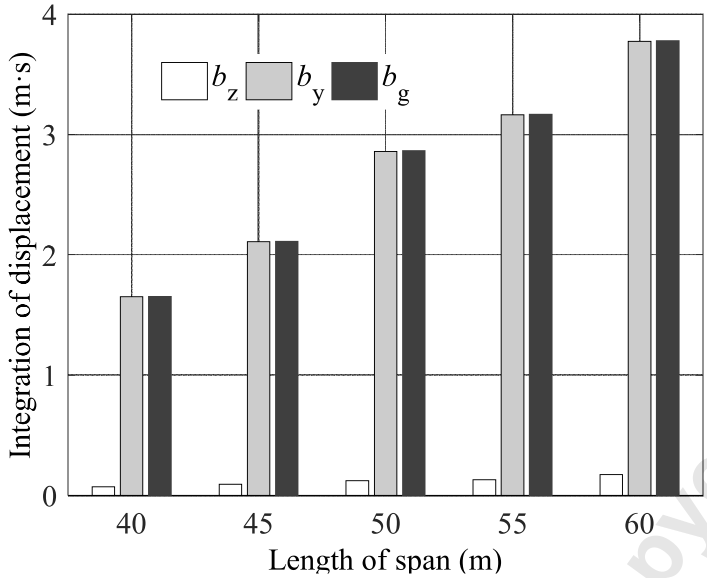

Figure 13. Results of integration of displacement with different lengths of span

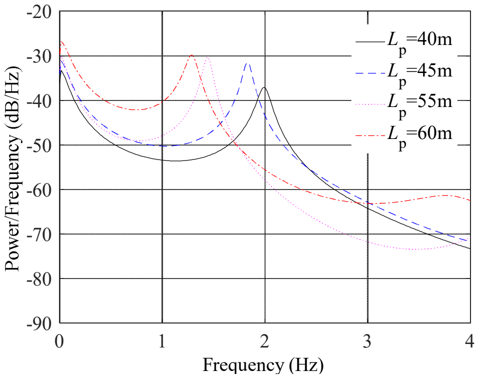

(a) Lateral vibration

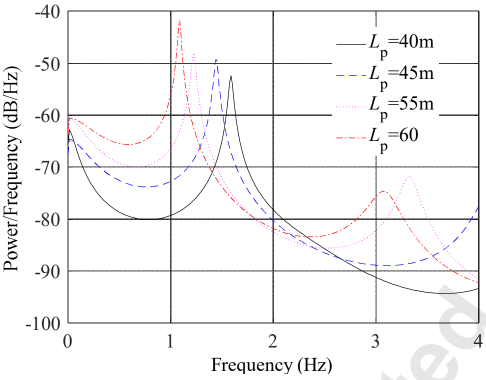

(b) Vertical vibration

Figure 14. Spectrums of the vibration response with different lengths of span with U= 20m/s

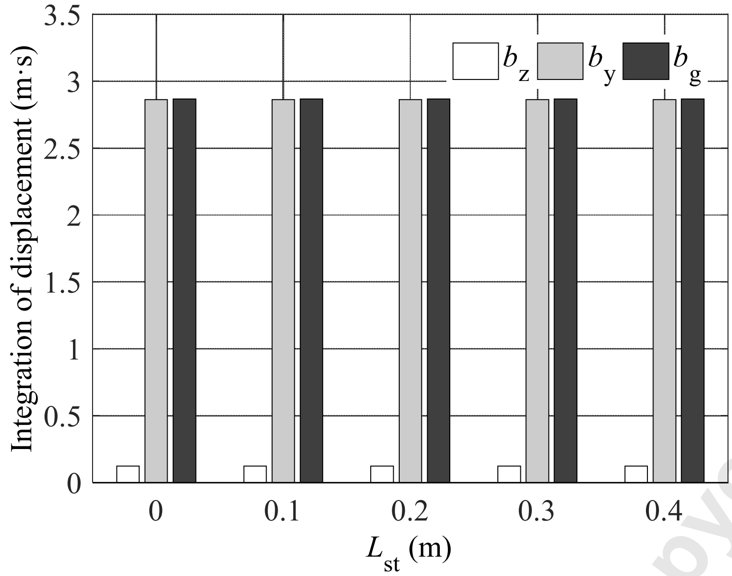

Figure 15. Results of integration of displacement with different stagger values

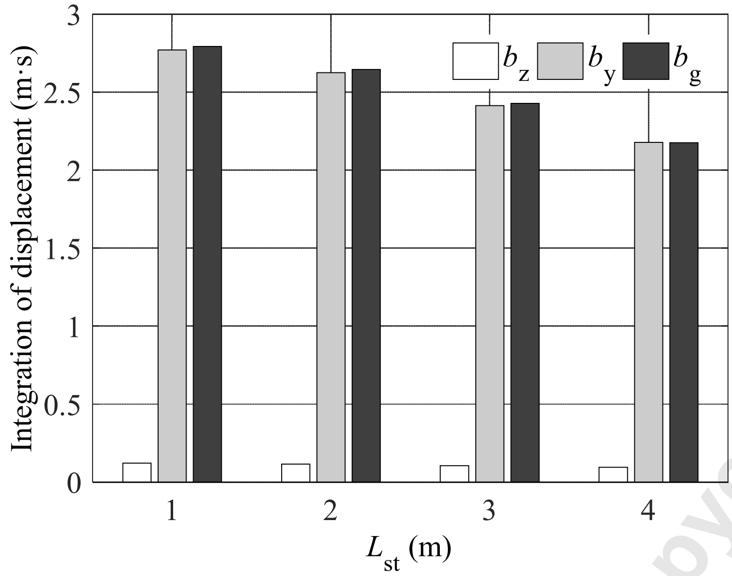

Figure 16. Results of integration of displacement with bigger stagger values

Journal of Vibration and Acoustics. Received January 15, 2017;
Accepted manuscript posted August 8, 2017. doi:10.1115/1.4037521

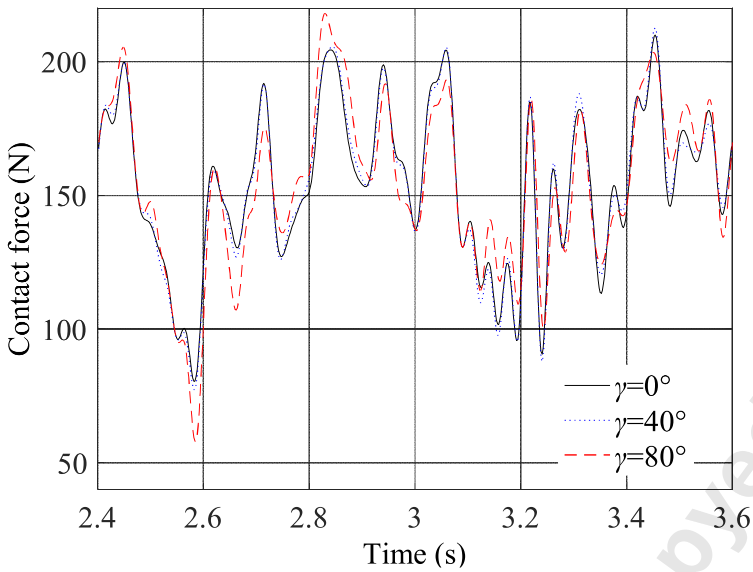

Figure 17. Results of contact force with different angles of wind deflection

Journal of Vibration and Acoustics. Received January 15, 2017;
Accepted manuscript posted August 8, 2017. doi:10.1115/1.4037521

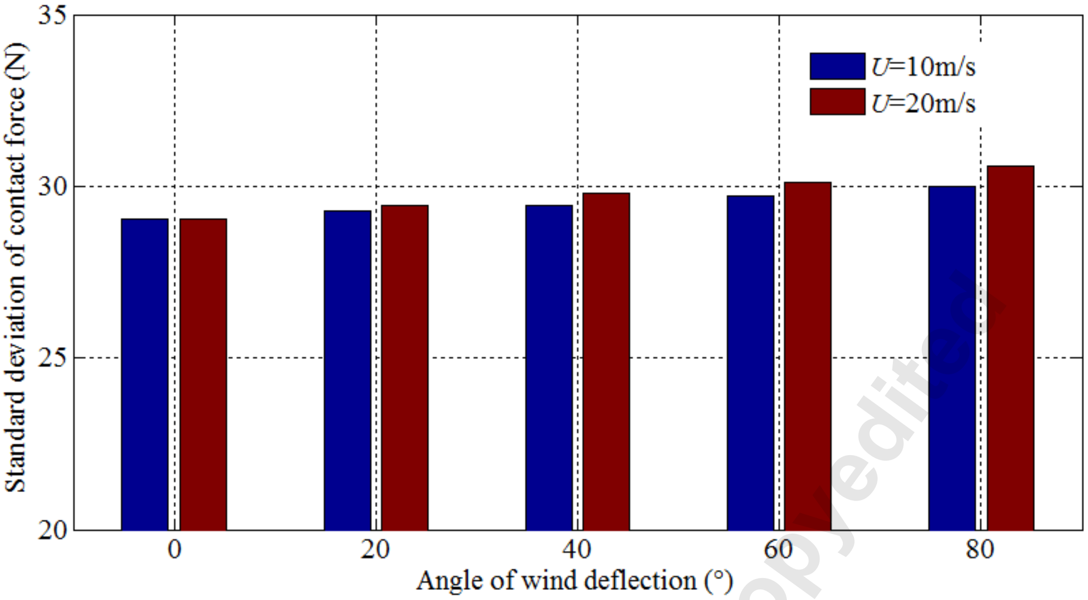

Figure 18. Standard deviations of contact force versus angle of wind deflection

Journal of Vibration and Acoustics. Received January 15, 2017;
Accepted manuscript posted August 8, 2017. doi:10.1115/1.4037521

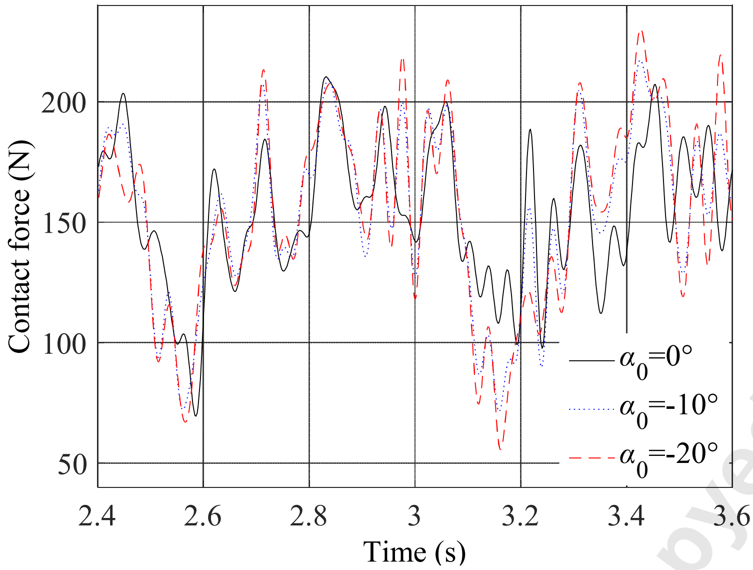

Figure 19. Results of contact force with different angles of attack

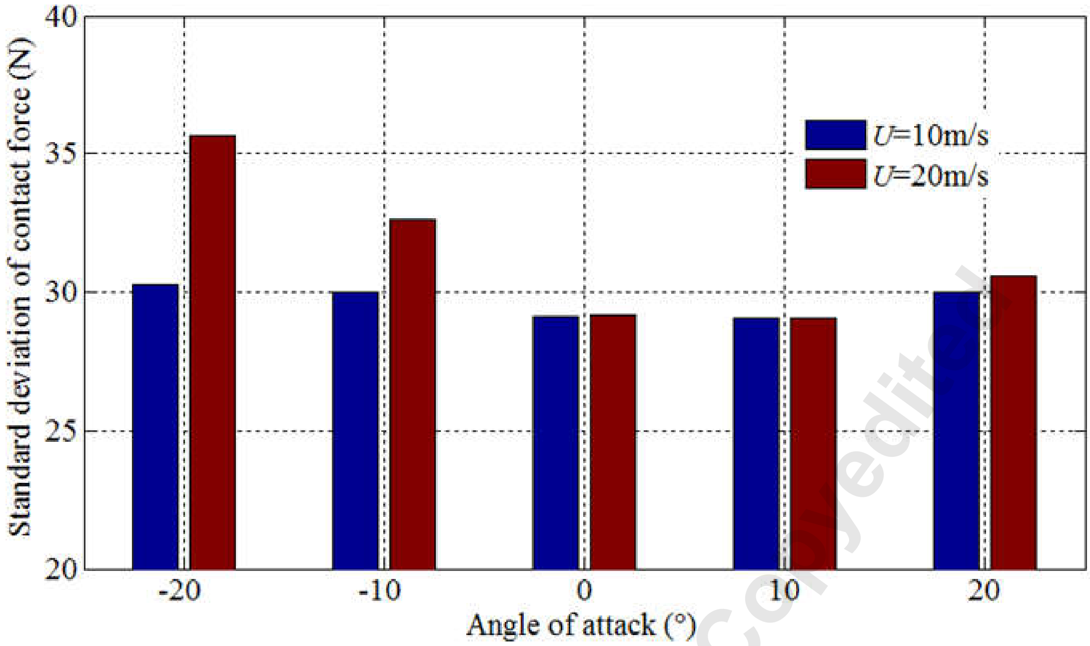

Figure 20. Standard deviations of contact force versus angle of attack

(a) Contact line model (b) Wind tunnel

Figure 21. Wind tunnel experiment for measuring aerodynamic coefficients

Table 1. Geometrical properties of catenary

Catenary material property	
Contact line	Line density: 1.082 kg/m; Tensile rigidity: 10^6 N/m; Tension: 27kN
Messenger line	Line density: 1.068 kg/m; Tensile rigidity: 10^6 N/m; Tension: 21kN
Dropper	Line density: 0.14 kg/m; Tensile rigidity: 10^5 N/m
Catenary geometrical property	
Encumbrance: 1.6m; Interval of droppers: 10m; Number of droppers: 5; Number of span: 10; Length of span: 50m; Stagger value: 0.3m; Steady arm stiffness: 1.25×10^7 N/m	

Journal of Vibration and Acoustics. Received January 15, 2017;
Accepted manuscript posted August 8, 2017. doi:10.1115/1.4037521

Table 2. Expressions of empirical spectrum in three directions [34-36]

Directions	Expressions of empirical spectrum
Along-wind	$S_{\mathrm{h}}(z,n)=\dfrac{200\overline{v}_{\mathrm{z}}^{2}f}{n(1+50f)^{5/3}}$; $f=\dfrac{nz}{\overline{v}_{\mathrm{z}}}$
Cross-wind	$S_{\mathrm{p}}(z,n)=\dfrac{13\overline{v}_{\mathrm{z}}^{2}f}{n(1+20.16f)^{5/3}}$; $f=\dfrac{nz}{\overline{v}_{\mathrm{z}}}$
Vertical-wind	$S_{\mathrm{v}}(z,n)=\dfrac{6\overline{v}_{\mathrm{z}}^{2}f}{n(1+4f)^{2}}$; $f=\dfrac{nz}{\overline{v}_{\mathrm{z}}}$

Journal of Vibration and Acoustics. Received January 15, 2017;
Accepted manuscript posted August 8, 2017. doi:10.1115/1.4037521

Table 3. First-order natural frequency

Lateral natural frequency (Hz)	Vertical natural frequency (Hz)
1.67	1.32

Table 4. First-order natural frequency with different contact wire tensions

r_t	Lateral natural frequency (Hz)	Vertical natural frequency (Hz)
0.8	1.39	1.27
0.9	1.48	1.29
1	1.67	1.32
1.1	1.69	1.39
1.2	1.82	1.43

Journal of Vibration and Acoustics. Received January 15, 2017;
Accepted manuscript posted August 8, 2017. doi:10.1115/1.4037521

Table 5. First-order natural frequency with different lengths of span

Length of span (m)	Lateral natural frequency (Hz)	Vertical natural frequency (Hz)
40	2.08	1.56
45	1.89	1.41
50	1.67	1.32
55	1.54	1.23
60	1.33	1.12

Journal of Vibration and Acoustics. Received January 15, 2017;
Accepted manuscript posted August 8, 2017. doi:10.1115/1.4037521

Table 6. Validation of the catenary-pantograph mode according to EN 50318 (only the 5th and 6th spans)

Statistical index	Ranges of the standard results		Computation results	
Speed [km/h]	250	300	250	300
Mean contact force (N)	110~120	110~120	118.30	118.06
Standard deviation (N)	26~31	32~40	26.72	34.87
Max. statistic value (N)	190~210	210~230	198.46	222.67
Min. statistic value (N)	20~40	-5~20	38.14	13.45
Max. real value (N)	175~210	190~225	191.13	208.04
Min. real value (N)	50~75	30~55	65.79	46.76
Max. uplift at support(mm)	48~55	55~65	52.06	60.73
Percentage of the loss of contact	0%	0%	0%	0%

Journal of Vibration and Acoustics. Received January 15, 2017;
Accepted manuscript posted August 8, 2017. doi:10.1115/1.4037521

Table 7. Drag coefficient C_D computed by wind tunnel experiment and CFD

	Wind speed（m/s）		
	5	10	20
Wind tunnel experiment	1.665	1.203	1.105
CFD	1.673	1.273	1.129